



How big is an OMI pixel?

Martin de Graaf^{1,3}, Holger Sihler², Lieuwe G. Tilstra³, and Piet Stammes³

¹Delft University of Technology, Delft, The Netherlands

²Max-Planck-Institute für Chemie, Mainz, Germany

³Royal Netherlands Meteorological Institute, De Bilt, The Netherlands

Correspondence to: M. de Graaf, graafdem@knmi.nl

1 Abstract.

2 The Ozone Monitoring Instrument (OMI) is a push-broom imaging spectrometer, observing solar
3 radiation backscattered by the Earth's atmosphere and surface. The shape of an OMI pixel is not
4 quadrangular, which is common for scanning instruments, but rather Gaussian-shaped as light from
5 neighbouring pixels enters the Field of View (FoV). This has consequences for pixel-area dependent
6 applications, like cloud fraction products, and visualisation.

7 The shape and sizes of OMI pixels were determined pre-flight by theoretical and experimental
8 tests, but never verified after launch. In this paper the OMI point spread function (PSF) is char-
9 acterised using collocated MODerate resolution Imaging Spectroradiometer (MODIS) reflectance
10 measurements. MODIS measurements have a much higher spatial resolution than OMI measure-
11 ments and spectrally overlap at 469 nm. The optimal OMI PSF was determined by finding the highest
12 correlation between MODIS and OMI reflectances for both cloud-free and partially clouded scenes.
13 Our results show that the semi-official OMPIXCOR product 75FOV corner coordinates accurately
14 fix the Full Width at Half Maximum (FWHM) of a super-Gaussian PSF, when this pixel shape is as-
15 sumed. The exponent of the super-Gaussian PSF is dependent on OMI pixel row number, from about
16 $n = 2$ at nadir to 3.5 at the swath edges, due to the increase in pixel size. The optimal Gaussian expo-
17 nent depends on scene changes between overpasses and reduces to about $n = 1$ for partially clouded
18 scenes before 2008. Then, the time difference between Aqua and Aura was 15 minutes instead of
19 8 minutes after 2008. Between overpasses, clouds change the scene, reducing the correlation and
20 changing the shape of the optimal overlap.

21 1 Introduction

22 The Ozone Monitoring Instrument (OMI) (Levelt et al., 2006) was launched in 2004 on-board the
23 Aura satellite, with the main objective to monitor trace gases in the Earth atmosphere, especially
24 ozone. It was built as the successor to the ESA instruments GOME (Burrows et al., 1999) and
25 SCIAMACHY (Bovensmann et al., 1999), and NASA's TOMS instruments (e.g. Fleig et al., 1986;
26 Bhartia et al., 2013). GOME and SCIAMACHY were the first space-borne hyperspectral instru-



27 ments, measuring the complete spectrum from the ultraviolet (UV) to shortwave-infrared (SWIR)
28 wavelength range with a relatively high spectral resolution (typically 0.2–1.5 nm), from which mul-
29 tiple trace gases, clouds and aerosol parameters can be retrieved simultaneously. TOMS instruments
30 have been monitoring the ozone column at a relatively high spatial resolution ($50 \times 50 \text{ km}^2$) with
31 daily global coverage since 1978. OMI was designed to combine those functions and measure the
32 complete spectrum from the UV to the visible wavelength range (up to 500 nm) with a high spatial
33 resolution and daily global coverage. To this end, the imaging optics were completely redesigned.

34 Instead of a rotating mirror, in OMI a two-dimensional CCD detector array (780×576 pixels) is
35 used to map the incoming radiation in the across-track and wavelength dimensions simultaneously. A
36 swath of about 2600 km in the across-track direction is imaged along one dimension of the detector
37 array. Spectrally, the radiation is split into a UV and a visible (VIS) channel and imaged along
38 the wavelength dimension of the detector array, giving a spectral resolution of 0.63 nm for the VIS
39 channel. The along-track direction is scanned due to the movement of the satellite. In default ‘Global’
40 operation mode, five consecutive CCD images, each with a nominal exposure time of 0.4 s, are
41 electronically co-added during a two second interval. The sub-satellite point moves about 13 km
42 during this time interval (Levelt, 2002). The consequence of this design is that the spatial response
43 function of the OMI footprints is not box-shaped, but has a peak at the centre of the footprint. This
44 new design, avoiding moving parts, was used in OMI for the first time, and is now being used in
45 several new upcoming satellite missions.

46 The telescope Field of View (FoV) is determined by the projection of the OMI spectrograph
47 slit on the Earth’s surface from the point of view of a CCD pixel. This projection is affected by the
48 imaging optics and is not a sharply bounded function, but consists of a central response function with
49 extending tails. The FoV has been determined pre-flight by measuring the intensity response to a star
50 stimulus for all pixels. This is proprietary information, but the results are summarised here. In the
51 swath (across-track) direction the average peak position for each pixel was determined and fitted to a
52 linear curve to determine the spatial sampling distance for the three channels. For the VIS channel the
53 FoV is 115.1° . The point spread function (PSF) in the across-track direction was not determined (or
54 reported). However, a memo from the OMI Science Support Team from 2005 shows an across-track
55 pixel size estimation from these measurements, where the sizes have been determined by assuming
56 no overlap between adjacent pixels and computing the distances between the peak positions when
57 imaged on the earth. This yields sizes in the across-track direction of 23.5 km at nadir and 126 km
58 for far off-nadir (56 degrees) pixels.

59 In the along-track direction the FoV was characterised by tilting the instrument to simulate the
60 movement in the flight direction. The measurements were fitted to a normal Gaussian curve with
61 variable width for different across-track angles and wavelengths. This width is reported as the Full
62 Width at Half Maximum (FWHM) in degrees, which is about 0.95 at nadir and 1.60 at 56 degrees for
63 the VIS channel. This corresponds to a nadir pixel size in the along-track direction of about 15 km



64 and a far off-nadir pixel size of about 42 km, when the Gaussian is convolved with the satellite
65 motion during 2 s.

66 The instantaneous FoV (iFoV) of the OMI instrument is influenced by a polarisation scrambler,
67 that transforms the incoming radiation from one polarisation state into a continuum of polarisation
68 states (as opposed to unpolarised light). The incoming beam is split into four beams of equal inten-
69 sity, scrambled, and projected onto the CCD. Since the projections of the four beams are slightly
70 shifted with respect to each other, the polarisation state of the incoming radiation still slightly deter-
71 mines the intensity distribution of the four beams and therefore the iFoV in the flight direction. The
72 only property which is not dependent on the polarisation state of the incoming radiation is the centre
73 of weight of the four beams. This corresponds to the centre of the ground pixels, which is therefore
74 the only geolocation coordinate that can be determined unambiguously (van den Oord, 2006).

75 Therefore, centre coordinates are provided in the Level 1b data product, but corner coordinates are
76 not. However, for mapping purposes, ground pixel area computations (e.g. for emission estimates per
77 unit area) and collocation, an OMI corner coordinate product was developed, called OMPICOR,
78 which is provided online via the OMI data portal (Kurosu and Celarier, 2010). Two sets of quadran-
79 gular corner coordinates are provided. One set contains *tiled* pixel coordinates, which are essentially
80 the midpoints between adjacent centre coordinates, mainly useful for visualisation purposes, as no
81 overlap between pixels is imposed. The other set contains so-called 75FOV pixel coordinates, which,
82 according to Kurosu and Celarier (2010), correspond to 75% of the energy in the along-track FoV.
83 The authors assumed a 1° FWHM for the iFoV to fix a Gaussian distribution and convolved it with
84 the satellite movement. The area under a Gaussian curve corresponds to about 76% at FWHM for a
85 normal distribution (exponent of 2), however, the authors claim to have used a super-Gaussian with
86 exponent of 4 for this. In this case the energy contained within the FWHM has increased to about
87 89%. When this iFoV is convolved with the satellite motion, the energy within the FWHM will have
88 increased even more. The 75FOV pixels generally overlap in the along-track direction, since radi-
89 ation emanating from adjacent swaths enter the FoV. The coordinates in the across-track direction,
90 however, are still the half-way points between adjacent pixels.

91 The application of quadrangular pixel shapes for OMI can become problematic when pixel values
92 are aggregated onto a regular grid (e.g. Level 3 products that are reported on a regular lat-lon grid).
93 If pixels overlap, which might occur when several orbits are averaged or in case of 75FOV pixels,
94 extreme values may be smoothed and reduced due to averaging. A more realistic distribution that
95 preserves mean values can be reconstructed using a parabolic spline surface on the quadrangular
96 grid, resulting in a much better visualisation (Kuhlmann et al., 2014). In cases where values from
97 OMI are compared with that of another instrument, especially with a higher spatial resolution, the
98 approximate true shape of an OMI pixel is desired. For example, we intend to combine spectral mea-
99 surements from OMI and MODIS to determine the aerosol direct effect over clouds (de Graaf et al.,



100 2012). To this end, an optimal characterisation of the PSF of the OMI footprint is desired, to optimise
101 the accuracy of the retrieval.

102 In this paper, the OMI PSF for the VIS channel is investigated by testing various predefined
103 shapes and sizes under various circumstances and determining the maximal correlation between
104 OMI and MODIS reflectances. In section 2, the consistency between overlapping OMI and MODIS
105 reflectances is investigated. A cloud-free scene from 2008 is used to study the PSF under the most
106 optimal circumstances. In chapter 3, a two dimensional super-Gaussian function with a varying expo-
107 nent is introduced, which can change shape from a near-quadrangular to a sharp-peaked distribution.
108 Furthermore, the sizes in both along and across-track directions can be varied. This function is used
109 to define various PSFs, which are investigated for various scenes. The change in PSF is further inves-
110 tigated by looking into the effect of scene and geometry changes during the (varying) overpass times
111 of OMI and MODIS. The conclusions from this study are reported in section 4. The geolocations of
112 the pixels in the UV channels are slightly different from those in the VIS channel. However, the PSF
113 cannot be determined in the same way for the UV, since MODIS measurements do not overlap with
114 these channels spectrally.

115 2 Data

116 Aura flies in formation with Aqua in the Afternoon constellation (A-train). Aqua was launched in
117 2002, to lead Aura in the A-train by about 15 minutes. The time difference between the instruments
118 within the A-train is controlled by keeping the various satellites within control-boxes, which are
119 defined as the maximum distances to which the satellites are allowed to drift before correcting ma-
120 noeuvres are executed. Therefore, the time difference between OMI and MODIS is variable by up
121 to a few minutes. A major orbital manoeuvre in 2008 of Aqua decreased the distance between the
122 Aura and Aqua control boxes to about 8 minutes.

123 To investigate the correlation between OMI and MODIS observed reflectances, several scenes
124 were selected. One reference scene will be discussed here in detail. It was an almost cloud-free
125 scene over the Sahara desert on 4 November 2008, around 14:00 UTC (start of the first MODIS
126 granule). At this point in time, the time difference between OMI and MODIS was reduced to 8
127 minutes and around 20 – 30 seconds, depending on the pixel row. The differences between the pixel
128 times arise from the fact that MODIS has a scanning mirror, while OMI has no scanning optics, but
129 exposes the CCD to different scenes while moving in the flight direction. The scene is visualised
130 in Figure 1, using MODIS channels 2, 1, and 3 to create an RGB picture at 1 km² resolution. The
131 MODIS granules are outlined in yellow, while the considered OMI scene is outlined in red. From
132 June 2007 onward, OMI suffered from a degradation of the observed signal in an increasing number
133 of rows, called the row anomaly (OMI row anomaly team, 2012). In November 2008 the anomaly
134 was limited to only rows 53 and 54 for scenes near the equator. These rows were disregarded in the



135 comparison. In order to stay within the MODIS swath the OMI swath was further reduced to rows 2
136 to 57. A total of 7,335 OMI pixels are left in the scene.

137 To compare reflectances from OMI and MODIS, the reflectance measured by OMI is convolved
138 with the MODIS spectral response function. MODIS channel 3 at 469 nm overlaps with the OMI
139 VIS channel (350 – 500 nm). This is illustrated in Figure 2, where two OMI reflectance spectra from
140 the VIS channel are plotted, together with the normalised MODIS response function of channel 3
141 (red curve). The reflectance spectra correspond to the darkest and brightest pixels (at 469 nm) in
142 Figure 1, indicated by the green boxes. The darkest pixel is a vegetated area with an OMI reflectance
143 of 0.0967 and the brightest pixel is a cloud covered scene with an OMI reflectance of 0.5075, both
144 at 469 nm.

145 All the 7,335 OMI pixels in the scene in Figure 1 were compared to collocated MODIS pixels, see
146 the left panel of Figure 3. Here, all the MODIS pixels that fall (partly) within an OMI quadrangular
147 pixel are averaged with equal weight, which is the easiest and quickest averaging strategy. The
148 MODIS reflectances show a Pearson's correlation coefficient r of 0.997 with the OMI reflectances,
149 and a standard deviation (SD) of 0.00433. The MODIS reflectances are somewhat lower than the
150 OMI reflectances; a linear fit through the points shows a slope of 0.954 and an offset of 0.0010.

151 3 OMI point spread function

152 The true PSF of an OMI pixel is expected to resemble a flat-top Gaussian shape. To investigate the
153 OMI PSF, the response at 469 nm is compared to the MODIS channel 3 signals, weighted using
154 different super-Gaussian functions in two dimensions, and checking the change in the correlation
155 and SD between the OMI and MODIS reflectances. A 2D super-Gaussian distribution is defined by

$$156 g(x, y) = \exp\left(-\left(\frac{x}{w_x}\right)^n - \left(\frac{y}{w_y}\right)^n\right), \quad (1)$$

157 where x and y are the along and across-track directions, and $w_{x,y}$ are the weights in either direction,
158 defined by

$$159 w_{x,y} = \frac{\text{FWHM}_{x,y}}{2(\log 2)^{1/n}}. \quad (2)$$

160 $\text{FWHM}_{x,y}$ are the full widths at half maximum in the along and across-track directions, respectively,
161 defined in this paper by the 75FOV pixel corner coordinates. The size of the PSF can be varied
162 to include more or fewer MODIS pixels from neighbouring pixels in the along and across-track
163 directions by varying $w_{x,y}$. All size changes are reported relative to $\text{FWHM}_{x,y}$.

164 The shape of the PSF is determined by the Gaussian exponent n , which defines the 'pointed-
165 ness' of the distribution, $n = 2$ corresponding to a normal distribution, $n < 2$ resulting in a point-hat
166 distribution and $n > 2$ resulting in a flat-top distribution, see the illustration in one dimension in
167 Figure 4. Various PSFs are illustrated in Figure 5. The colours of the square MODIS pixels indi-
168 cate the relative contribution of that pixel. Figure 5a shows the quadrangular OMI pixel, with all



169 MODIS pixels within the OMI corner coordinates having equal weight, while all pixels outside the
170 footprint have zero weight. Figure 5b shows a 2D flat-top super-Gaussian ($n = 8$) shape resembling
171 the quadrangular shape but with smoother edges, and using the 75FOV corner coordinates to fix the
172 FWHM. Figure 5c shows a normally or 2D Gaussian ($n = 2$) distribution, while Figure 5d shows
173 a 2D point-hat super Gaussian ($n = 1$) distribution. Figures 5e and f show the weights for pixels
174 which are assumed to be twice as wide or long as the 75FOV pixels and using a 2D normal Gaussian
175 distribution.

176 The size and shape of the assumed PSF was varied in steps of $0.25n$ and $0.25 \cdot \text{FWHM}$ for a wide
177 range of these parameters, and for each configuration the correlation between the OMI and MODIS
178 reflectances and the SD was determined, using all pixels from the scene in Figure 1. The correlation
179 change is shown in Figure 6. The blue curve shows the change in correlation for a changing exponent
180 n , and $1 \cdot \text{FWHM}$, i.e. the change in PSF shape and fixed 75FOV corner coordinates. In this case, the
181 highest correlation is obtained when a Gaussian distribution with exponent $n = 2.5$ is used, which
182 is slightly more flat-topped than a normal distribution. The red lines show the change in correlation
183 when the shape of the distribution is fixed to a normal distribution ($n = 2$). In that case, the corre-
184 lation peaks for an across-track width of $0.8 \cdot \text{FWHM}$, corresponding to a slightly more narrow pixel
185 in the across-track direction. In the along-track direction the correlation peaks at $1 \cdot \text{FWHM}$. If all
186 three parameters are allowed to vary at the same time, the maximum correlation is found as before:
187 $n = 2.5$ and the pixel sizes corresponding to the 75FOV corner coordinates in both directions. This
188 is shown by the purple curve, which shows the variation along the across-track direction for the op-
189 timal parameters. Obviously, the maximum in the purple curve is the same as the one for the blue
190 curve: $r = 0.9974$. This is higher than the correlation when quadrangular pixels are used.

191 The correlation between the OMI and MODIS reflectances and the SD, when the optimal PSF for
192 this scene is used, is shown in the right panel of Figure 3. The SD for the optimal PSF is 0.00409.
193 The change in SD for different shapes and sizes is not shown, because it is consistent with the change
194 of the reciprocal of the correlation, in the sense that it is minimal when the correlation peaks and can
195 be equally used to find the optimal PSF in this way.

196 3.1 PSF sensitivity

197 So, when a super-Gaussian form is assumed, the optimal OMI PSF for the reference scene can be
198 characterised using an exponent $n = 2.5$ and 75FOV corner coordinates for the Gaussian FWHM.
199 However, the correlation between OMI and MODIS reflectances is not a constant. A number of
200 scenes were investigated to show the change in correlation between OMI and MODIS reflectances
201 in time and space. They are treated below and illustrated in Figures 7 – 9.

202 First, another cloud-free scene was found over the Middle East on 7 October 2008, starting on
203 10:20 UTC, see Figure 7. The time difference between OMI and MODIS is about 8 minutes and 34–
204 45 s. This scene is entirely cloud-free over land, and the reflectance ranges from 0.12 over the ocean



205 to 0.41 over the desert. The correlation between the OMI and MODIS reflectances is depicted in the
206 right panel of Figure 7, which displays the same dependencies as in Figure 6. The highest correlation
207 ($r = 0.9965$) using 75FOV corner coordinates is found for a Gaussian distribution with an exponent
208 of $n = 3$ (blue line). When the shape is fixed to a normal distribution ($n = 2$), the highest correlation
209 ($r = 0.9964$) is found for pixel sizes that are smaller (0.8-FWHM) in the across-track direction, as
210 for the reference scene. This is also the absolute maximum and therefore the red across-track curve
211 coincides with the purple one.

212 Next, a scene over Australia was selected on 11 October 2008 starting on 04:45 UTC, see Figure 8.
213 The time difference between OMI and MODIS is also about 8 minutes and 35–43 s. This scene has
214 a large cloud-free part. Most cloud pixels, indicated by the red rectangles, were not used in the
215 analysis. The correlation between OMI and MODIS for various shapes and sizes is again displayed
216 in the right panel. The maximum correlation for this scene was $r = 0.9907$, obtained for a point-
217 hat Gaussian distribution with exponent $n = 1.75$ and FWHM corner coordinates. Note that the
218 correlation is significantly lower than for the reference scene.

219 Lastly, another Sahara cloud-free scene in the beginning of 2008 was selected, shown in Figure 9.
220 At this time the correcting manoeuvre bringing OMI closer to MODIS had not yet been performed
221 and the time difference between the instruments is as large as around 14 minutes, up to 16 minutes
222 and 26 s. The highest correlation is found for a Gaussian distribution with an exponent of $n = 1.5$
223 (blue line), which is a point-hat super-Gaussian distribution with wide wings. Similarly, when the
224 shape is fixed to a normal distribution ($n = 2$), the highest correlation is found for pixel sizes that are
225 wider than the 75FOV corner coordinates, which is different from the reference scene in Figure 1.
226 The most striking difference, however, is the much lower absolute value of the correlation. The
227 maximum correlation for this scene is $r = 0.980$, which is 2% lower than for the reference scene,
228 in December 2008. Even a 4 times wider pixel size in the reference scene yields a much higher
229 correlation between the OMI and MODIS. Apparently, the time difference between the Aqua and
230 Aura of 15 minutes makes a comparison between the two instruments much more challenging, even
231 for almost cloud-free scenes. It is unlikely that the OMI FoV has changed much between January
232 and December 2008. Furthermore, a cloud-free Sahara scene in 2006 (31 January 2006, around
233 13:55 UTC, not shown), showed the same lower correlation, peaking for a Gaussian exponent $n = 1$,
234 which is also a point-hat distribution with wide tails. The maximum correlation for this scene was
235 $r = 0.971$, which is in the same order as this scene in January 2008.

236 3.2 Scene dependencies

237 The effect of changing scenes between overpasses can be illustrated by looking at the pixels with the
238 highest SD between the OMI reflectances and the average collocated MODIS reflectances. Even for
239 a scene after 2008, when the overpass time difference is reduced to about 8 minutes, the retrieved
240 TOA reflectance can change significantly during this time in the case of broken clouds. The pixels



241 with the highest SD for the reference scene were marked blue in the right panel of Figure 3. The
242 marked points correspond to the blue coloured OMI pixels in Figure 1, which are the areas where
243 the scene contains broken cloud fields. In the few minutes between Aqua and Aura overpasses these
244 clouds change shape and position, changing the average reflectance in a pixel when the cloud fraction
245 is changed.

246 This is the main reason for the small optimal super-Gaussian exponent for the 2006 Sahara scene
247 (Figure 9): due to scene changes during the different overpass times, the observed overlap function
248 deviates from the true PSF, which closely resembles a Gaussian or flat-topped Gaussian. Instead
249 a more point-hat distribution with wider wings is found. The centre of the pixel becomes more
250 important, since this point will still have the highest correlation for both instruments. But since the
251 signal becomes more spread out, the wider wings give a higher correlation than the true PSF.

252 3.3 Viewing angle dependence

253 The 2008 Australian scene also has the highest correlation for an exponent smaller than 2, but the
254 presence of clouds only partly explains this. Most of the cloud pixels were removed, but keeping
255 those pixels in the correlation experiment increased the optimal Gaussian exponent, to 2.5, rather
256 than decreasing it. The reason for this is that the OMI PSF is dependent on the pixel row, and the
257 PSF is wider at the swath ends. Most of the cloud pixels are at the swath ends, and removing these
258 pixels removes the larger exponents. This viewing angle dependence is treated here.

259 Since the OMI FoV is dependent on the polarisation of the scene, the PSF should also be depen-
260 dent on the scattering geometry. To demonstrate this, the OMI PSF was determined as a function of
261 viewing zenith angle (VZA). For all the scenes described above, the optimal super-Gaussian shape
262 was determined per OMI pixel row, by varying the Gaussian exponent and determining the maxi-
263 mum correlation between OMI and MODIS pixels for each pixel row. Then the optimal exponents of
264 all five scenes presented above were averaged and plotted as a function of pixel row. In this analysis,
265 the 75FOV pixel sizes were used, to reduce the number of variables and because the above analy-
266 sis showed that the 75FOV corner coordinates are good indicators of the pixel sizes for Gaussian
267 shapes. The result is shown in Figure 10. The function shows a very erratic behaviour, due to the
268 rather large steps in Gaussian exponents nodes that were used ($0.25n$), while the change in correla-
269 tion for a change in Gaussian exponent is very small near the optimum. As a consequence, the pixel
270 shape has only a limited sensitivity near the optimum, and the retrieved Gaussian exponent is rather
271 wildly fluctuating. Averaging over the scenes reduces this, but is somewhat arbitrary. In Figure 10 a
272 boxcar average over 5 neighbouring points is shown as well.

273 A general trend can be observed from a flat-topped Gaussian shape towards the edge of the swath
274 with an exponent of about 3.5 to an exponent of around 2 at nadir. Next to the fact that the OMI
275 FoV is polarisation dependent, the reason for the increasing exponent towards the swath edges is the
276 pixel size increase towards the swath edges. The pixel sizes are shown for reference. The OMI pixel



277 sizes increase dramatically towards the edge for the across-track direction. Wide pixels have smooth
278 edges and a flat interior, while the small pixels around nadir also have smooth edges, but are too
279 small to display a flat interior. The left and right edges are just ‘glued’ together. This is expressed by
280 a Gaussian exponent of 2 or even lower.

281 This effect is in the across-track direction only, since the pixel size change in the along-track
282 direction is much smaller. A Gaussian shape which is fixed in the along-track direction and variable
283 in the across-track direction will probably give an even higher correlation, but this was not attempted.

284 3.4 Geometry differences

285 The correlation between OMI and MODIS reflectances at 469 nm shows that OMI reflectances
286 are consistently about 5% larger than the aggregated MODIS reflectances (see Figure 3). These
287 differences can be governed by changes in viewing and solar conditions between OMI and MODIS.
288 Since the optics and sub-satellite points differ for both instruments, the viewing angles are slightly
289 different, even if the satellites roughly follow the same orbit. More importantly, since Aura is always
290 behind Aqua, the solar zenith angle for OMI is always different from that of MODIS.

291 To investigate the effect of the differences in scattering geometry on the measured TOA re-
292 flectance, a cloud-free Rayleigh reflectance was modelled for each OMI pixel in the reference scene
293 in Figure 1. Each pixel was simulated twice, once using the OMI scattering geometry and once using
294 an average MODIS scattering geometry. In this way the expected reflectance difference can be de-
295 termined due to the difference in overpass time, keeping all else the same. To determine the average
296 MODIS reflectance, the simulated radiances were averaged over the OMI footprint using the optimal
297 flat-top Gaussian distribution with $n = 2.5$, as was determined for this scene (Figure 6). The average
298 radiance was then divided by the cosine of the solar zenith angle of the MODIS pixel which is closest
299 to the centre of the OMI pixel. In this way, the most representative solar zenith angle is used to nor-
300 malise the radiances. A realistic surface albedo was taken for each pixel, in order to make the model
301 results comparable to the observations. The surface albedo database used was the TERRA/MODIS
302 spatially completed snow-free diffuse bihemispherical land surface albedo database (Moody et al.,
303 2005). The monochromatic calculations were performed at 469 nm, using a standard Rayleigh at-
304 mosphere (Anderson et al., 1986) reaching to sea level, and an ozone column of 334 DU. The results
305 are shown in Figure 12.

306 The reflectance ranges from about 0.085 to 0.28, depending on the surface albedo, which is smaller
307 than the observed reflectances (cf. Figure 3, right panel). This is mainly due to the clouds in the scene
308 which are not simulated. The simulated OMI reflectances are larger than the simulated MODIS re-
309 flectances due to different geometries, like the observations. However, the difference for the simu-
310 lations, with a slope of 0.9965 and an offset of -0.001 , is much smaller than for the observations.
311 Therefore, we conclude that geometry differences between OMI and MODIS introduce differences
312 of less than 1% and cannot explain the observed slope between OMI and MODIS reflectances. Most



313 likely, calibration differences are causing the difference between the observed reflectances. The sim-
314 ulated correlation and SD are also notably better than for the observed scene. As noted before, clouds
315 have the largest impact on the correlation between the observed reflectances of a scene.

316 3.5 Accuracy of combining OMI and MODIS

317 The optimal PSF of OMI can now be determined for practical purposes, i.e. mixed scenes with
318 ocean, land and clouds. This is needed to determine the accuracy that can be expected when OMI
319 and MODIS measurements are combined to reconstruct the reflectance spectrum for the entire short-
320 wave spectrum. To determine the accuracy, the correlation between collocated OMI and MODIS
321 reflectances and the SD was determined by comparing the instruments for the scene shown in Fig-
322 ure 11. This scene was taken on 13 June 2006, starting on 13:33 UTC when the time difference
323 between the instruments was about 15 minutes. The scene contains a mixture of land and ocean
324 scenes, with and without clouds, and also smoke from biomass burning on the African continent.
325 Only OMI rows 10–50 were processed, which will often be the case to avoid problems with large
326 pixels or extreme viewing angles. The optimal correlation was found for a Gaussian exponent $n = 1$
327 and 75FOV corner coordinates (not shown). The low Gaussian exponent can be explained from the
328 presence of clouds that change the scene between the overpasses, and the exclusion of wide pixels
329 at the swath edges. The correlation between the OMI and MODIS reflectances using this shape is
330 shown in the right panel of Figure 11. Obviously, the correlation is a lot lower than for cloud-free
331 scenes ($r = 0.963$). The SD is 0.0373, which must be taken into account when OMI and MODIS
332 reflectances are compared or combined. Furthermore, the slope of a linear fit between the OMI and
333 MODIS reflectance is 0.909, which is smaller than that for cloud-free scenes, which showed about
334 5% difference. This larger range in reflectances for cloud scenes apparently off-sets the difference
335 between the instruments even further.

336 4 Conclusions

337 The correlation between OMI and collocated MODIS reflectances was determined, to inter-compare
338 the performance of the instruments and to find the PSF of the OMI footprint. MODIS channel 3 at
339 469 nm overlaps with OMI's visible channel, and the signals can be compared when the reflectance
340 signal of OMI is convolved with the MODIS spectral response function, and MODIS reflectances
341 are aggregated over the OMI footprint.

342 Due to the design of the OMI CCD detector array and the optical path, the footprint of OMI is
343 not quadrangular and light from neighbouring pixels enters the OMI FoV. The shape and size of the
344 footprint was determined for a cloud-free scene, to eliminate as much as possible scene changes due
345 to the different overpass times of Aura and Aqua. Assuming a super-Gaussian shape with variable
346 exponent and FWHM, the best characterisation of the OMI PSF is found for an exponent $n = 2 - 2.5$



347 and 75FOV corner coordinates to define the FWHM. When the corner coordinates are fixed, the
348 Gaussian exponent ranges from about 2 at nadir to about 3.5 at the swath edges. This is partly
349 because the OMI PSF is dependent on polarisation, due to the presence of a polarisation scrambler.
350 Therefore, the OMI PSF changes as a function of viewing angle. However, the main reason is the
351 increase in pixel size for off-nadir angles. For very wide pixels the signal flattens at the centre. This
352 effect may become more pronounced when the super-Gaussian exponent in the across-track direction
353 is made independent of the one in the along-track direction.

354 The OMI-MODIS overlap function is scene dependent. In particular, for larger time differences
355 between the Aqua and Aura overpasses, the optimal overlap function shape is found for smaller
356 Gaussian exponents n , still with the FWHM at the 75FOV corner coordinates. When the scene
357 changes between overpasses the signal is spread over a larger area, centred around the centre coor-
358 dinate. Therefore, a more optimal overlap function is found for a point-hat distribution with wider
359 wings. This is especially true for cloud scenes, which are most frequent. The correlation decreases,
360 and the SD increases, when clouds are in the scene, and this can be used as an indication of the
361 expected accuracy of a comparison between OMI and MODIS reflectances. For a scene with broken
362 clouds over both land and ocean in 2006, an optimal Gaussian exponent of $n = 1$ was found. How-
363 ever, in general, the changes in correlation coefficient are small for small changes of the Gaussian
364 exponent around 2 (much smaller than e.g. changes due to different time differences). Therefore
365 we recommend that the OMI PSF is approximated by a normal Gaussian distribution with exponent
366 $n = 2$ and 75FOV corner coordinates, as a trade-off between the reduction of the exponent because
367 of scene changes (clouds), and the increase of the exponent at the swath edges.

368 In all of the investigated cases the OMPICOR 75FOV corner coordinates adequately fix the size
369 of the pixel.

370 The use of non-scanning optics like that used in OMI will be continued in new instruments, in
371 particular TropOMI/Sentinel-5P (Veefkind et al., 2012), to be launched in 2016. For TropOMI, a
372 cloud masking feature is anticipated from Suomi-NPP/VIIRS (Schueler et al., 2002). Sentinel-5P
373 will fly in ‘loose formation’ with Suomi-NPP, with expected overpass time differences of about
374 5 minutes. The results from this study are relevant for that mission, since such an overpass time
375 difference will significantly change the overlap function between TropOMI and VIIRS, and affect
376 the accuracy of a cloud mask from VIIRS. High resolution VIIRS measurements can be used in the
377 way presented in the present paper to study and characterise the TropOMI PSF and the accuracy of
378 the cloud mask.

379 *Acknowledgements.* This project was funded by the Netherlands Space Office, project no.: ALW-GO/12-32.

380 Three anonymous referees are thanked for their constructive remarks on the draft manuscript.

381 **References**

- 382 Anderson, G. P., Clough, S. A., Kneizys, F. X., Chetwynd, J. H., and Shettle, E. P.: AFGL Atmospheric con-
383 stituent profiles, Tech. Rep. AFGL-TR-86-0110, Air Force Geophysics Laboratory, 1986.
- 384 Bhartia, P. K., McPeters, R. D., Flynn, L. E., Taylor, S., Kramarova, N. A., Frith, S., Fisher, B., and DeLand,
385 M.: Solar Backscatter UV (SBUV) total ozone and profile algorithm, Atmos. Meas. Tech., 6, 2533–2548,
386 doi:10.5194/amt-6-2533-2013, 2013.
- 387 Bovensmann, H., Burrows, J. P., Buchwitz, M., Frerick, J., Noël, S., Rozanov, V. V., Chance, K. V., and
388 Goede, A. P. H.: SCIAMACHY: Mission Objectives and Measurement Modes, J. Atmos. Sci., 56, 127–150,
389 doi:10.1175/1520-0469, 1999.
- 390 Burrows, J. P., Weber, M., Buchwitz, M., Rozanov, V., Ladstätter-Weissenmayer, A., Richter, A., DeBeek,
391 R., Hoogen, R., Bramstedt, K., Eichmann, K. -U., Eisinger, M., and Perner, D.: The Global Ozone Mon-
392 itoring Experiment (GOME): Mission Concept and First Scientific Results, J. Atmos. Sci., 56, 151–175,
393 doi:10.1175/1520-0469, 1999.
- 394 de Graaf, M., Tilstra, L. G., Wang, P., and Stammes, P.: Retrieval of the aerosol direct radiative
395 effect over clouds from spaceborne spectrometry, J. Geophys. Res., 117, doi:10.1029/2011JD017160,
396 <http://dx.doi.org/10.1029/2011JD017160>, 2012.
- 397 Fleig, A. J., Bhartia, P. K., Wellemeyer, C. G., and Silberstein, D. S.: Seven years of total ozone from the TOMS
398 instrument-A report on data quality, Geophys. Res. Lett., 13, 1355–1358, doi:10.1029/GL013i012p01355,
399 1986.
- 400 Kuhlmann, G., Hartl, A., Cheung, H. M., Lam, Y. F., and Wenig, M. O.: A novel gridding algo-
401 rithm to create regional trace gas maps from satellite observations, Atmos. Meas. Tech., 7, 451–467,
402 doi:10.5194/amt-7-451-2014, 2014.
- 403 Kurosu, T. P. and Celarier, E. A.: OMIPIXCOR Readme File, available at:
404 http://disc.sci.gsfc.nasa.gov/Aura/data-holdings/OMI/documents/v003/OMPIXCOR_README_V003.pdf,
405 2010.
- 406 Levelt, P. F.: OMI Instrument, Level 0-1b processor, Calibration & Operations, in: OMI Algorithm Theoretical
407 Basis Document. Volume I, 2002.
- 408 Levelt, P. F., van den Oord, G. H. J., Dobber, M. R., Mälkki, A., Visser, H., de Vries, J., Stammes, P., Lundell,
409 J. O. V., and Saari, H.: The ozone monitoring instrument, IEEE T. Geoscience and Remote Sensing, 44,
410 1093–1101, 2006.
- 411 Moody, E. G., King, M. D., Platnick, S., Schaaf, C. B., and Gao, F.: Spatially complete global spectral surface
412 albedos: Value-added datasets derived from Terra MODIS land products., IEEE Trans. Geosci. Remote Sens.,
413 43, 144–158, 2005.
- 414 OMI row anomaly team: Background information about the Row Anomaly in OMI,
415 <http://projects.knmi.nl/omi/research/product/rowanomaly-background.php>, 2012.
- 416 Schueler, C. F., Clement, J. E., Ardanuy, P. E., Welsch, C., DeLuccia, F., and Swenson, H.: NPOESS VIIRS
417 sensor design overview, in: Proc. SPIE, vol. 4483, pp. 11–23, doi:10.1117/12.453451, 2002.
- 418 van den Oord, G. H. J.: OMI Field of View, OMI Science Team Document RP-OMIE-KNMI-XYZ, Issue draft,
419 January 2006, 2006.

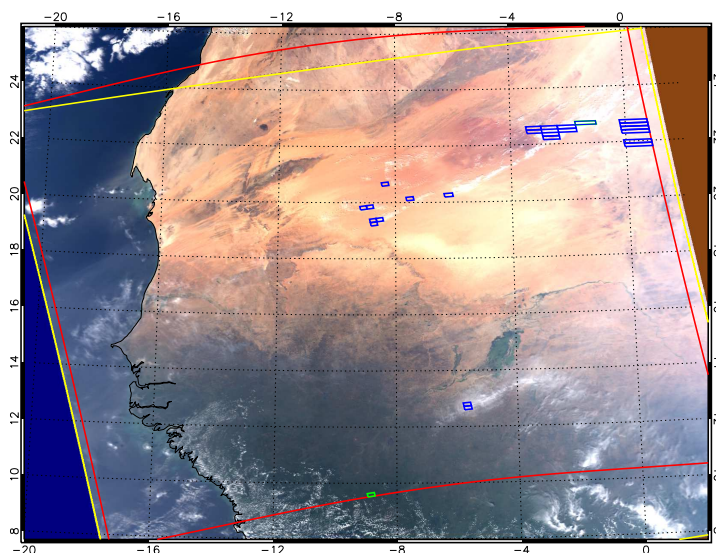


Figure 1. MODIS RGB image of the reference scene on 4 November 2008, 14:00 UTC (start of the lower MODIS granule). The yellow lines indicate the MODIS data granules and the red lines the considered OMI swath, which was confined to rows 2 – 57, with the exception of pixels in the row anomaly (see text). The green pixels indicate the darkest (vegetated) and the brightest (cloud covered) areas in the scene. The OMI reflectance spectra of these pixels are shown in Figure 2. The blue OMI pixels correspond to the blue marked points in Figure 3.

420 Veefkind, J., Aben, I., McMullan, K., Förster, H., de Vries, J., Otter, G., Claas, J., Eskes, H., de Haan, J.,
421 Kleipool, Q., van Weele, M., Hasekamp, O., Hoogeveen, R., Landgraf, J., Snel, R., Tol, P., Ingmann, P.,
422 Voors, R., Kruizinga, B., Vink, R., Visser, H., and Levelt, P.: TROPOMI on the ESA Sentinel-5 Precursor:
423 A GMES mission for global observations of the atmospheric composition for climate, air quality and ozone
424 layer applications, *Remote Sens. Environ.*, 120, 70–83, 2012.

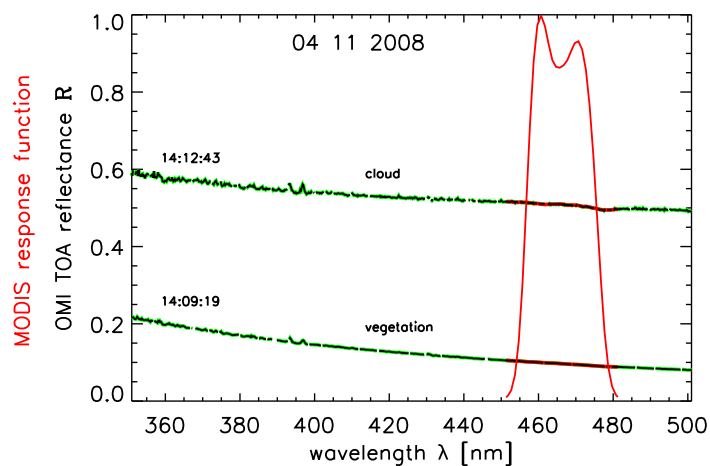


Figure 2. OMI top-of-atmosphere reflectance spectra on 4 November 2008, 13:37:24 UTC, and 13:38:02 UTC, of the green pixels in Figure 1 (black/green); and the normalised MODIS response function of channel 3 (red).

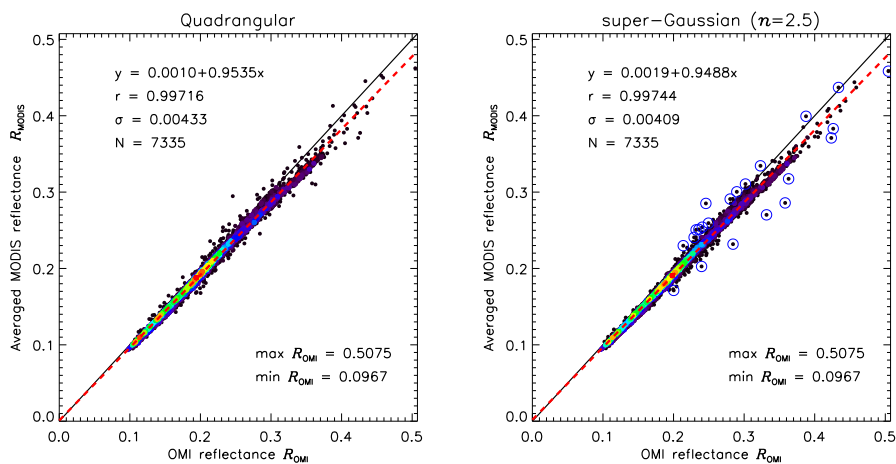


Figure 3. Scatter plot of OMI and MODIS collocated reflectances for the scene in Figure 1 using quadrangular OMI pixels (left panel) and optimised super-Gaussian ($n = 2.5$) pixels (right panel). The red dashed line is the linear least squares fit to the measurements, given by the linear function $y = a_0 + a_1x$ in the plot. r is Pearson's correlation coefficient and σ the standard deviation. The blue marked points have the largest σ and correspond to the blue OMI pixels in Figure 1. N is the number of points and $\max R_{\text{OMI}}$ and $\min R_{\text{OMI}}$ the maximum and minimum value in the plot, respectively.

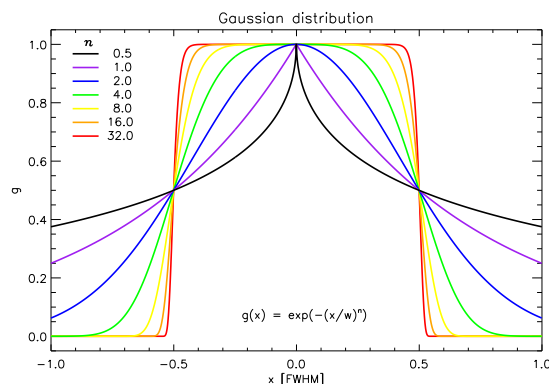


Figure 4. One dimensional normalised super-Gaussian distribution functions with varying exponents n . The normal distribution ($n = 2$) is plotted in blue.

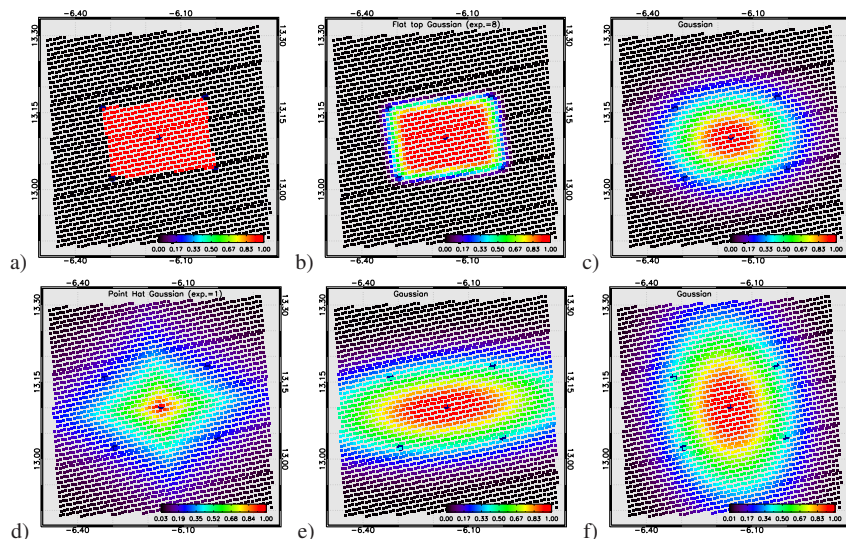


Figure 5. OMI 75FOV corner coordinates (dark blue filled circles), with the OMI centre coordinate (dark blue diamond), and collocated MODIS centre coordinates (black and coloured squares). The colours of the squares indicate the weighting of the MODIS pixels as indicated by the colour bar. From top left in reading order: Quadrangular, with all MODIS pixels within the corner coordinates having equal weights, everything else disregarded; a 2D flat top Gaussian with exponent $n = 8$, resembling the rectangle with smoothed edges; a 2D Gaussian or normal distribution; a 2D point-hat Gaussian distribution with exponent $n = 1$; a 2D Gaussian distribution with twice the width in the across-track direction; a 2D Gaussian distribution with twice the width in the along-track direction.

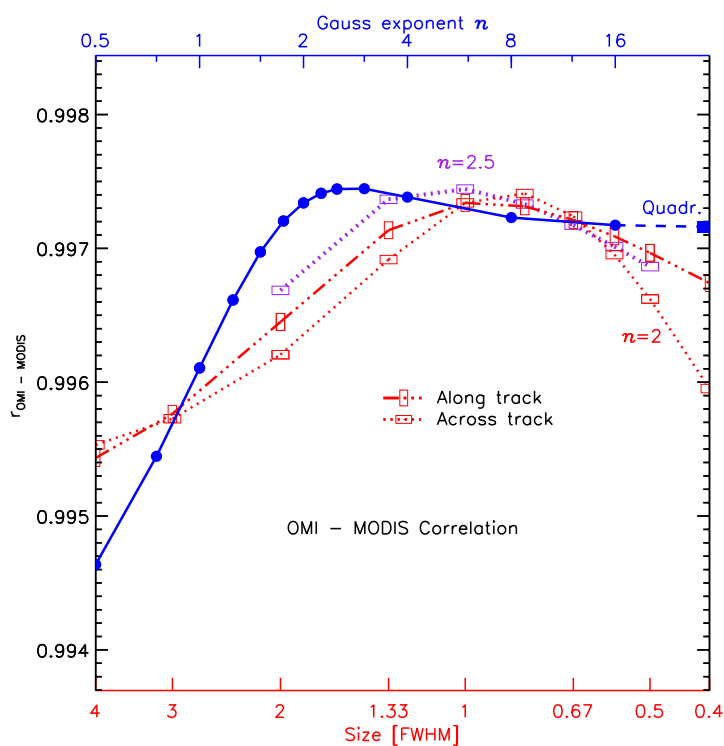


Figure 6. Dependence of Pearson's correlation coefficient r between the OMI and MODIS observed reflectance for the scene in Figure 1 as a function of super-Gaussian shape and size. The blue line indicates the relationship as a function of exponent n , for fixed 75FOV corner coordinates. The red lines are the relationships for varying pixel sizes when a Gaussian exponent $n = 2$ is chosen. The purple line indicates r as a function of across-track size for the optimal along-track and Gaussian exponent. In this case the optimum was for a Gaussian exponent $n = 2.5$ and 1-FWHM in both directions.

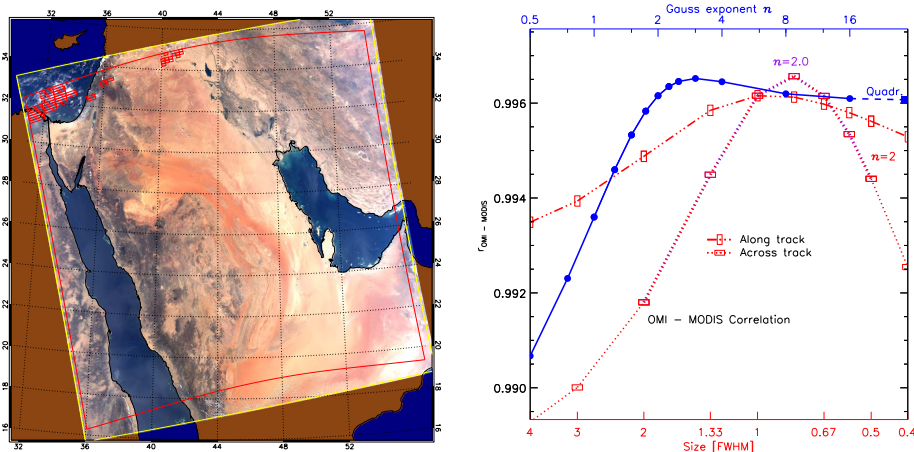


Figure 7. Left panel: MODIS RGB scene on 7 October 2008, 10:20 UTC over the the Middle East. Yellow and red lines as in Figure 1, while the individual red OMI pixels are cloud pixels that were manually discarded. Right panel: Dependence of Pearson's correlation coefficient r between the OMI and MODIS observed reflectance for the scene in the left panel as a function of super-Gaussian shape and size, as in Figure 6. The optimum in this case was found for a Gaussian exponent $n = 3$ and $1 \times 75\text{FOV}$ corner coordinates in both directions, or $n = 2$ and the across-track size = $0.8 \times 75\text{FOV}$.

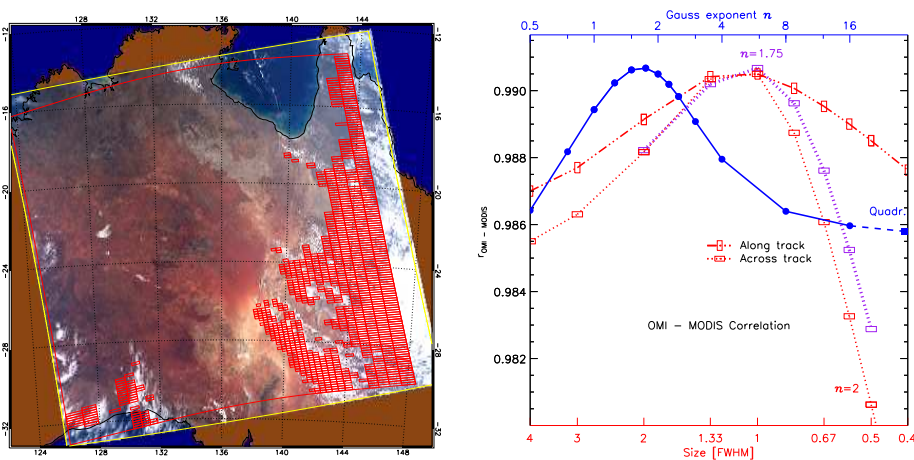


Figure 8. Same as Figure 7 on 11 October 2008, 04:45 UTC over Australia. The optimum in this case was found for a Gaussian exponent $n = 1.75$ and $1 \times 75\text{FOV}$ corner coordinates in both directions.

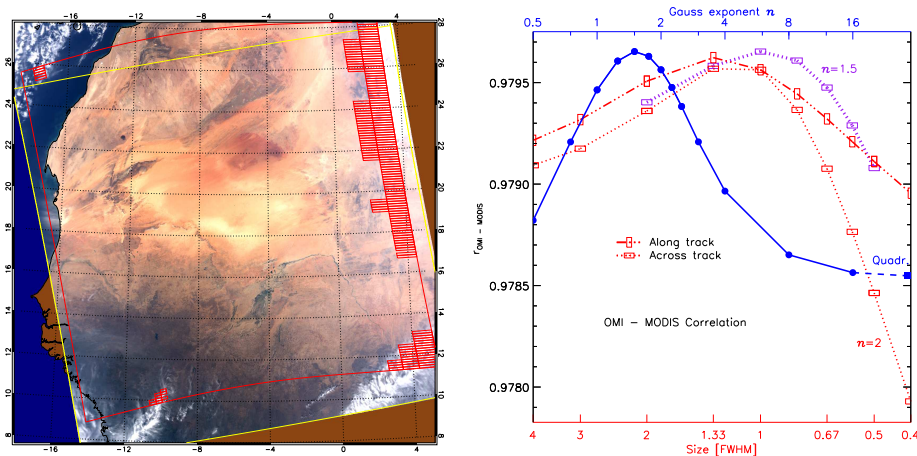


Figure 9. Same as Figure 7 on 7 January 2008, 13:45 UTC over the Sahara desert. The optimum in this case was found for a Gaussian exponent $n = 1.5$ and $1 \times 75\text{FOV}$ corner coordinates in both directions.

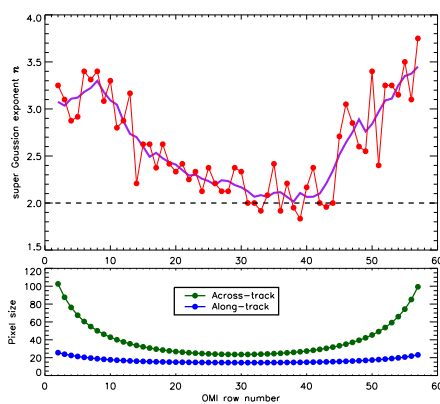


Figure 10. Super-Gaussian exponent as a function of OMI pixel row, averaged over all scenes introduced in this paper (red). The FWHM was fixed to the 75FOV pixel sizes, shown in the lower panel, to determine the optimal exponent. The purple curve is the boxcar average of the red curve, using 5 points.

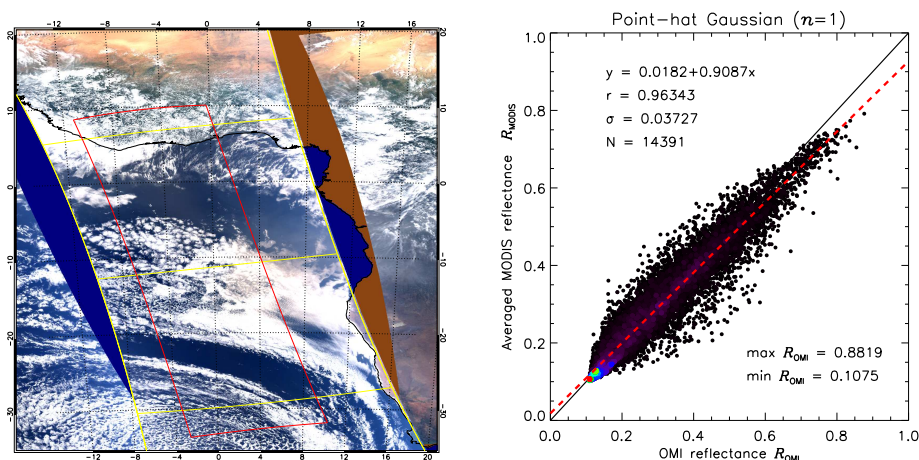


Figure 11. MODIS RGB image on 13 August 2006, around 13:33 UTC (lower part of the image). The yellow lines indicate the MODIS data granules and the red lines the considered OMI swath, which was from rows 10 – 50. The optimal correlation between OMI and MODIS for this scene was found for a Gaussian exponent $n = 1$ and 75FOV corner coordinates. The correlation for this pixel shape is shown in the right panel.

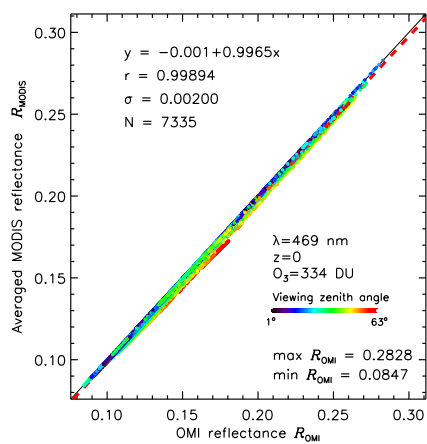


Figure 12. Simulated clear-sky reflectances for the reference scene in Figure 1 using OMI scattering geometries (x -axis) and MODIS geometries (y -axis). The colours indicate the OMI viewing zenith angle of each simulated pixel. The reflectances were simulated at 469 nm, for a standard atmosphere reaching to sea level, and an ozone column of 334 DU. The surface albedo was varied according to a database (see text). The underlying red dashed line shows the linear fit to the simulations.